Progress In Electromagnetics Research C, Vol. 79, 159–173, 2017

Design of RF Sensor for Simultaneous Detection of Complex Permeability and Permittivity of Unknown Sample

Pratik Porwal[1, *], Azeemuddin Syed[1], Prabhakar Bhimalapuram[2], and Tapan Kumar Sau[2]

Abstract—In this paper, a novel microwave planar resonant sensor is designed and developed for simultaneous detection of permittivity and permeability of an unknown sample using a nondestructive technique. It takes advantage of two-pole filter topology where the interdigitated capacitor (IDC) and spiral inductor are used for placement of a sample with significant relative permittivity and permeability values. The developed sensor model has the potential for differentiating permittivity and permeability based on the odd mode and even mode resonant frequencies. It operates in the ISM (industrial, scientific and medical) frequency band of 2.2–2.8 GHz. The sensor is designed using the full wave electromagnetic solver, HFSS 13.0, and an empirical model is developed for the accurate calculation of complex permittivity and permeability of an unknown sample in terms of shifts in the resonant frequencies and transmission coefficients (S_{21}) under loaded condition. The designed resonant sensor of size $44\times24\,\text{mm}^2$ is fabricated on a 1.6 mm FR4 substrate and tested, and corresponding numerical model is experimentally verified for various samples (e.g., magnetite, soft cobalt steel (SAE 1018), ferrite core, rubber, plastic and wood). Experimentally, it is found that complex permeability and permittivity measurement is possible with an average error of 2%.

1. INTRODUCTION

The field of sensing and characterization of an unknown sample is an imperative area of biology, solid state physics, material science and electronics engineering. The traditional chemical methods used for sensing are cumbersome (several reaction steps), time consuming, destructive and requires large volume of testing sample [1–3]. As a result in recent years, cell scale analysis using electrochemical, optical, piezoelectric, thermal, or mechanical principles which falls under electronics, optics, and informatics categories becomes influential tools in the clinical diagnostic field [4]. All these tools allow rapid, sensitive, real time measurements, and these techniques are label-free [5]. Therefore, the nondestructive sensing using RF and microwave frequency is an effective technique.

There are different RF sensing techniques available, which are categorized under the nonresonant and resonant methods [6]. The nonresonant methods are normally used for wide-band characterization of samples with moderate accurate results [7]. Therefore, the resonant methods are preferred over nonresonant methods for obtaining accurate results over a narrow band of operation. Among the resonant methods, the sensing and characterization of a sample can be performed either using rectangular waveguide cavity resonator [8], H-slot cavity resonator [9] or with the help of planar resonant sensors [10]. Since cavity resonator technique requires bulky and costly metallic cavity, the planar resonant sensors are preferred because of advantages such as low cost, easy fabrication and integration with other microwave circuits [11]. Designs of the planar resonant sensor are mostly based on various

Received 4 September 2017, Accepted 31 October 2017, Scheduled 13 November 2017

* Corresponding author: Pratik Porwal (email@affiliation.com).

[1] Center of VLSI and Embedded System Technology (CVEST), IIIT, Hyderabad-500032, India. [2] Center for Computational Natural Sciences and Bioinformatics (CCNSB), IIIT, Hyderabad-500032, India.

resonant structures such as split ring resonators (SRR) [12–15], complementary split ring resonators (CSRR) [16], substrate integrated waveguide (SIW) [17, 18], slotline based RF sensor [19], stepped impedance resonator (SIR) [20], series resonators [21], fractal capacitors [22], spiral inductors [23] and interdigitated capacitor (IDC) [24]. Among these different resonant structures, the fractal capacitors, spiral inductors, IDC are easy to get fabricated on microstrip line and provide a reasonably high amount of sensitivity. On the contrary, in the case of the SRR and CSRR structures, the resonant structure is coupled to the microstrip line either electrically or magnetically depending upon the orientation of the resonator with the microstrip line [25], thus reducing their sensitivity.

RF resonant sensors find variety of applications in estimating the permittivity of different polar and non-polar organic chemical solvents, detection of adulteration in oils and permeability of magnetic particles present in a sample, haemoglobin in blood [26], etc. However, two different resonant sensors [27, 28] are required to sense permittivity and permeability independently. This makes the system complicated and increases its cost and size.

In this paper, a planar resonant RF sensor based on a combination of spiral inductor and IDC structure is proposed for simultaneous detection of permittivity and permeability of an unknown sample. The proposed structure is etched on the main microstrip line for getting the maximum sensitivity, and the basic design is carried out using the HFSS 13.0. The design specifications of each individual structure and corresponding frequency response of both even and odd quasi Tranverse Electromagnetic (TEM) mode are derived for the proposed design. The numerical data obtained from the finite integration technique based approach are used to develop an empirical model of the proposed sensor. The developed numerical model is used to calculate the real part and tangent loss of the permittivity and permeability of a sample on the basis of shift in odd and even mode resonant frequencies and transmission coefficients. This proposed sensor of size 44 mm $\times$ 24 mm is fabricated on a 1.6 mm thick FR-4 substrate operating in the frequency range of 2.2–2.8 GHz. The resonant frequency and magnitude of the transmission coefficient of the magnetic and dielectric samples are measured using the vector network analyzer (VNA) and analysed in detail. The measurement of various standard samples (i.e., magnetite, soft cobalt steel, ferrite core, rubber, plastic and wood) using proposed sensor ensures that the error in calculation of complex permittivity and permeability is around 2%.

2. PROPOSED DESIGN OF RF RESONANT SENSOR

The proposed RF resonant sensor is designed using two spiral inductors and IDC as shown in Fig. 1(a). The spiral inductors are connected in series with IDC, whereas both spiral inductors are also in series through underpass as shown in Fig. 1(b) and Fig. 1(c). For testing procedures, the unknown sample is placed at the spacing between two inductors and IDC fingers such that it covers the most sensitive area of the sensor. The basic series RLC circuit model of the proposed sensor is as shown in Fig. 1(d).

The series resonant branches of L_{IDC} C_g model the two halves of the IDC, where C_g presents the capacitive effect between the metallic halves through ground plane, and L_g models the inductive paths of IDC structure. Here, C_m stands for the mutual capacitive effect between the IDC fingers. Spiral inductor is in series with IDC, and the corresponding inductance is denoted by L_{Ind}. These coupled inductors and capacitor interact with each other through electrical and magnetic couplings.

2.1. Design Specifications

Spiral inductor and IDC are the chief constituents of the proposed design, and each element is discussed as follows.

2.1.1. IDC Structure

The structure of IDC is shown in Fig. 2. The coplanar geometry can be transformed into a parallel plate geometry using conformal transformation technique [29]. The capacitance of IDC (C_{IDC}) can now be calculated as

$$C_m = nx(C_1 + C_2)\,\text{pF}, \tag{1}$$

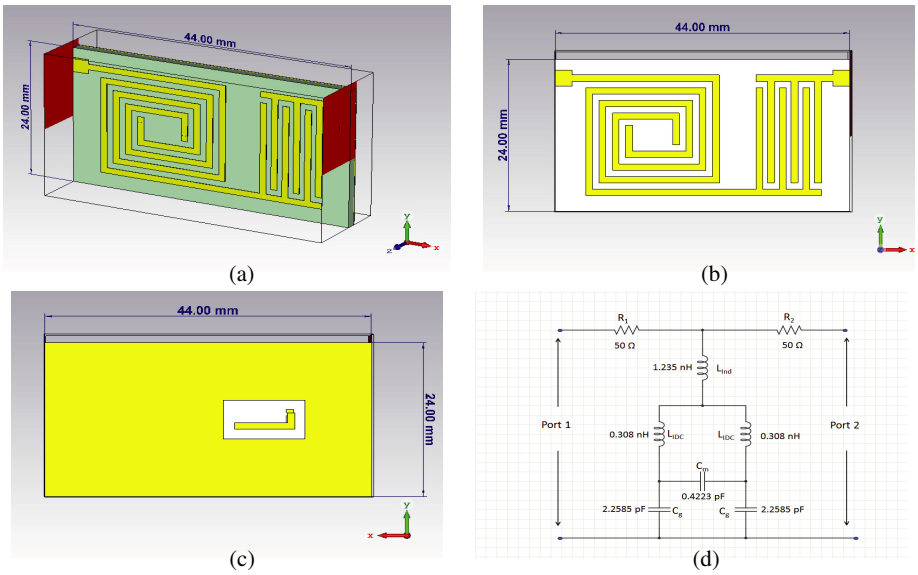

Figure 1. (a) 3D view and (b) metal layer view of proposed biosensor design using two spiral inductor and Interdigitated capacitor (c) layout of the ground plane (d) electrical circuit model of proposed sensor.

x	Length of finger	10 mm
a	Width of finger	1 mm
d	Spacing between fingers	0.75 mm
n	No of fingers	6
h	Height of a substrate	1.6 mm
ϵ_{sub}	Dielectric constant of a substrate	3.9
ϵ'_r	Dielectric constant of a test sample	—

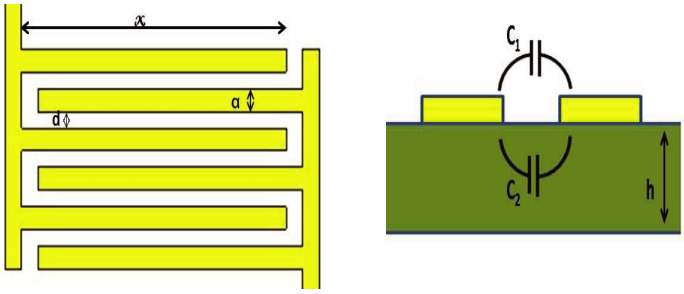

Figure 2. (a) Top view and (b) cross sectional view of IDC structure.

where x is the length of IDC finger, n the total number of fingers, and C_1 and C_2 are the line capacitance of coplanar strip with air and dielectric substrate, respectively. C_1 and C_2 are given as [29]

$$C_1 = 4\epsilon_0\epsilon'_r \frac{K(k'_1)}{K(k_1)} \text{ pF/cm}, \tag{2}$$

$$C_2 = 2\epsilon_0(\epsilon_{sub} - 1)\frac{K(k'_2)}{K(k_2)} \text{ pF/cm}, \tag{3}$$

$$k_1 = \left(1 + \frac{2a}{2d+a}\right)\left(\sqrt{\frac{1}{1+\frac{2a}{d}}}\right), \tag{4}$$

$$k_1' = \sqrt{1-k_1^2}, \tag{5}$$

$$k_2' = \frac{\sinh\left(\frac{\pi a}{4h}\right)}{\sinh\left(\frac{\pi}{2h}\left(\frac{a}{2}+d\right)\right)} \times \sqrt{\frac{\sinh^2\left(\frac{\pi}{2h}\left(\frac{3a}{2}+d\right)\right) - \sinh^2\left(\frac{\pi}{2h}\left(\frac{a}{2}+d\right)\right)}{\sinh^2\left(\frac{\pi}{2h}\left(\frac{3a}{2}+d\right)\right) - \sinh^2\left(\frac{\pi a}{4h}\right)}}, \tag{6}$$

$$k_2 = \sqrt{1-k_2'^2}, \tag{7}$$

$$\frac{K(k)}{K(k')} = \frac{2}{\pi}\ln\left(2\sqrt{\frac{1+k}{1-k}}\right). \tag{8}$$

Here, $K(k)$ is a complete elliptical integral of the first kind.

2.1.2. Inductor Design

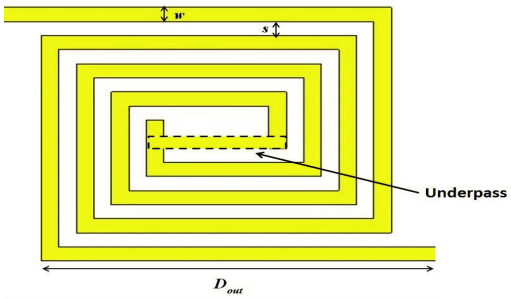

D_{out}	outer dimension of spiral	10 mm
w	Line Width	1 mm
s	Spacing between lines	1 mm
N	No of turns	2

Figure 3. Design of two spiral inductor connected through underpass.

The structure of two spiral inductors is as shown in Fig. 3. Both spiral inductors are in series and connected through underpass. For such a symmetrical structure, the total length (l_{tot}) of the inductor is given by [30]

$$l_{tot} = 4N\left(D_{out} - w - (N-1)(w+s)\right), \tag{9}$$

where, N is the number of turns, D_{out} the outer diameter of spiral, w the metal width, and s the spacing between segments. The total inductance of an inductor consists of the inductor self-inductance (L_{self}) and of the remaining part, which comes from the total negative (M^-) and total positive (M^+) mutual inductances that include all negative and positive interactions among all segments of inductor. The self-inductance of the square inductor can be expressed as [30]

$$L_{self} = 2\times10^{-7}\times l_{tot}\times\ln\left(\frac{l_{tot}}{w} + 1.193 + 0.2235\frac{w}{l_{tot}}\right)\text{ H}. \tag{10}$$

The expressions for mutual inductances are simple and easy to understand resulting from the symmetry properties of the square geometry. The total negative mutual inductance can be expressed as [31]

$$M^- = 0.47\times\frac{\mu}{2\pi}\times N\times l_{tot} \quad H. \tag{11}$$

The third constitutive element of the total inductance is the total positive mutual inductance. The average distance (d^+) for the constituting factor of positive mutual inductance can be calculated by

$$d^+ = \frac{(w+s)(N+1)}{3} \tag{12}$$

The total positive mutual inductance is [32]

$$M^{+} = \frac{\mu}{2\pi} \times l_{tot} \times (N-1) \times \left(\ln\left(\sqrt{1+p^2}+p\right) - \left(\sqrt{1+\left(\frac{1}{p}\right)^2}+\frac{1}{p}\right)\right) \text{ H}, \tag{13}$$

where

$$p = \frac{l_{tot}}{4Nd^{+}} \tag{14}$$

Thus, the total inductance (L_{tot}) of the spiral inductor is given as

$$L_{tot} = L_{self} + M^{+} - M^{-} \text{ H}. \tag{15}$$

2.2. *E*-Field and *H*-Field Analysis

The sensor design takes advantage of two-pole filter topology, and IDC allows electromagnetic energy transfer from one port to the other. The electric field is strong and homogeneous between fingers of the IDC, whereas magnetic field is strong and homogeneous across the inductor as shown in Fig. 4. The electric field between fingers is 2.677×10^3 V/m and near inductor is 4.321×10^2 V/m. Since very weak electric field is experienced near the surface of the inductor as compared to IDC, the area between fingers is the most sensitive region for detection of permittivity. On the contrary, magnetic field across the inductors is 2.93 A/m and is minimum at IDC area. Therefore, the gap between inner diameters of two inductors is the most sensitive region for detection of permeability of a sample.

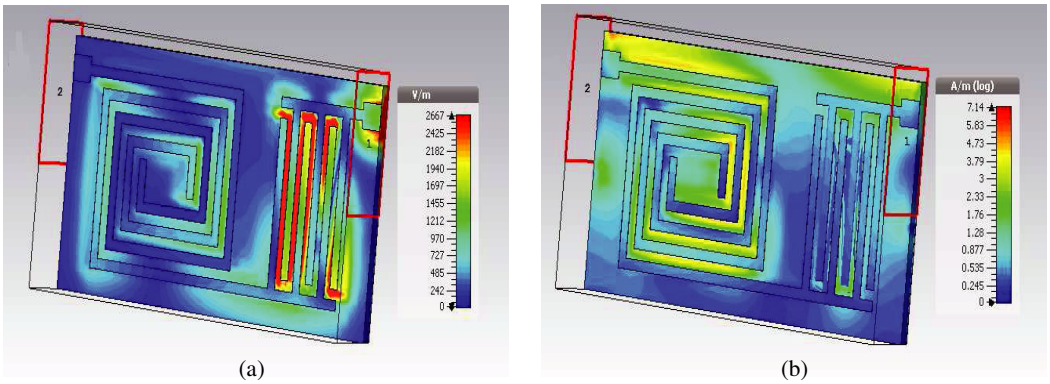

(a) (b)

Figure 4. (a) Electric field distribution and (b) magnetic field distribution at the surface of proposed sensor.

2.3. Frequency Response of Proposed Sensor

Figure 2 illustrates the cross section of a pair of coupled microstrip lines (IDC strucure) under consideration in this section, where these microstrip lines of width a are in the edge-coupled configuration with a separation d. Therefore, this structure supports two quasi-TEM modes, i.e., the even mode and odd mode. Frequency response of the sensor is same as that of the dual-bandstop RF filter. It has two resonant frequencies, which are separated from each other as shown in Fig. 5. These two resonant frequencies are due to propagation of odd mode and even mode [33]. These two TEM modes of wave propagation can be characterized by the even mode characteristic impedance Z_e and odd mode characteristic impedance Z_o. Z_e is defined as the characteristic impedance between one line and the ground when equal and in phase voltages are impressed on the two lines, and Z_o is defined as the characteristic impedance between one line and the ground when equal but opposite phase voltages are impressed. The propagation constants and phase constant for these modes are given by [34]

$$\gamma_{o,e} = \left[(Y_0 \pm Y_m)(Z_0 \mp Z_m)\right]^{1/2}, \tag{16}$$

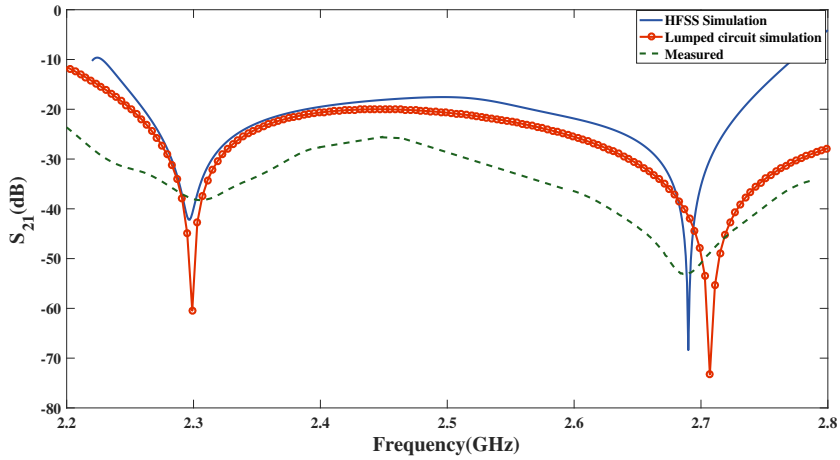

Figure 5. Simulated and measured frequency response of proposed sensor.

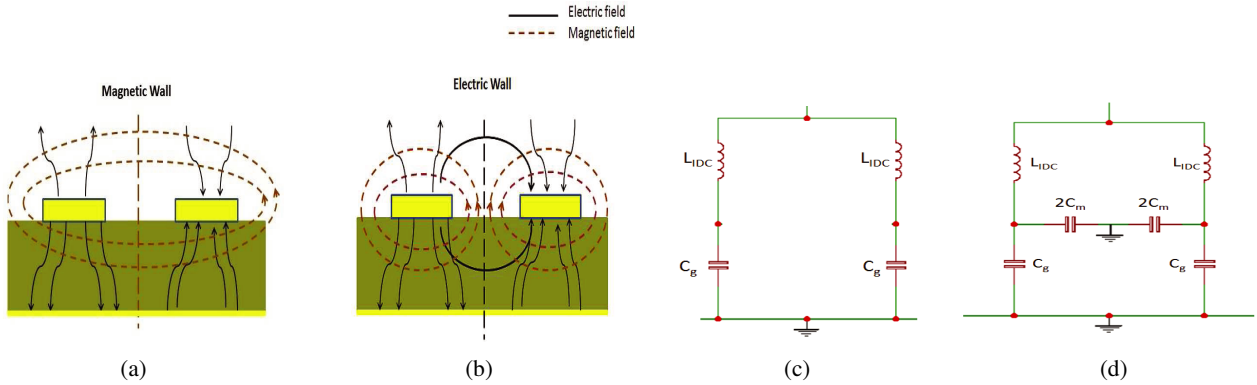

Figure 6. (a) Electric and magnetic field distributions at even mode. (b) Electric and magnetic field distributions at odd mode. (c) Even-mode circuit model of IDC. (d) Odd-mode circuit model of IDC.

where, Y_0 and Y_m are the self and mutual admittances, and Z_0 and Z_m are the self and mutual impedances. The propagation constant is a complex quantity, and it is given by [35],

$$\gamma_{o,e} = \alpha_{o,e} + j\beta_{o,e}, \tag{17}$$

where, $\alpha_{o,e}$ is the attenuation constant and $\beta_{o,e}$ the phase constant

$$\beta_{o,e} = \omega \left(L_0 C_0 - L_m C_m \pm (L_m C_0 - L_0 C_m)\right)^{1/2} \text{ rad/m}. \tag{18}$$

The impedances of odd mode and even mode are given by [36]

$$Z_e = \frac{\omega}{\beta_e}(L_0 - L_m)\,\Omega, \tag{19}$$

$$Z_o = \frac{\beta_o}{\omega}\left(\frac{1}{C_0 + C_m}\right)\Omega. \tag{20}$$

The impedance lines are characterized by inductance per unit length L_0 and capacitance per unit length C_0. L_m is the mutual inductance, C_m the mutual capacitance, and ω the operating frequency.

Electric and magnetic field distributions in design at odd mode and even mode are as shown in Figs. 6(a) and 6(b). The even mode only depends on the magnetic coupling, and the resonant frequency (f_e) is more sensitive to the inductors, whereas the odd mode mainly relies on the electric coupling and its frequency (f_o) changes as a function of the interdigitated capacitance value. It can be inferred from

Fig. 2 (equivalent circuit) that the particle can exhibit the even and odd-mode resonances with the equivalent circuits demonstrated in Figs. 6(c) and 6(d), respectively. In the even mode, the two halves of the resonator have the same voltage distribution. Thus, and no current will pass through C_m, and it will be open-circuited. Conversely, in the odd mode, there will be a virtual ground across the electric wall, and CM is broken into two equal parts of $2C_m$. Based on Fig. 2, Fig. 7(c), Fig. 7(d) and the above discussion, the even- and odd-mode resonance frequencies can be defined as

$$f_e = \frac{1}{2\pi\sqrt{((L_{IDC} + L_{Ind}))C_g}}\,\text{Hz}, \tag{21}$$

$$f_o = \frac{1}{2\pi\sqrt{((L_{IDC} + L_{Ind}))(C_g + 2C_m)}}\,\text{Hz}. \tag{22}$$

3. SIMULATION RESULTS AND NUMERICAL MODELING

In this section, we discuss frequency response of the designed sensor before and after addition of a sample with different permeabilities and permittivities at different positions on sensors.

3.1. Addition of Sample with Significant Relative Permeability

After modeling the sensor, the magnetic samples (mangetite, SAE 1018, Ferrite core) having permeability between 1–20 are added in the sensor, and corresponding shifts in the resonant frequency are observed for each permeability value as compared to the unloaded case of the sensor as shown in Fig. 7. Moreover, the magnitude of even-mode frequency shift is directly proportional to the permeability value of the sample. Table 1 gives details of the frequency shifts for permeability values of test samples. After observation of different shifts in resonant frequency for variation in relative permeability, the empirical formula derived using Equations (1)–(15) and (21) for determining the real part of permeability

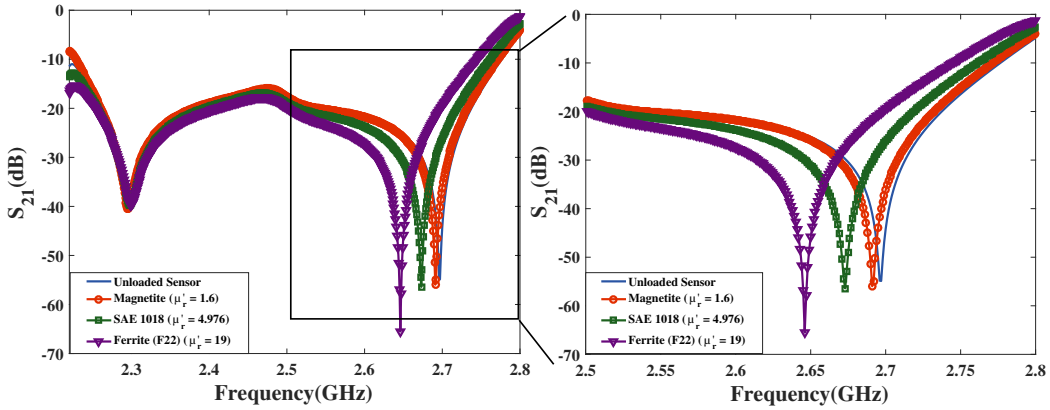

Figure 7. Frequency response of the sensor before and after addition of sample with different permeability value.

Table 1. Even mode resonant frequency shifts after addition of different permeability.

Test sample	Relative permeability	Even mode resonant frequency Shift
Magnetite	1.6	4.5 MHz
SAE 1018	4.976	24 MHz
Ferrite core (F22)	19	45 MHz

is given by,

$$\mu_r' = \frac{1}{1.16}\left(\frac{30.7648}{(2.969 - 0.040487 \times \Delta f)^2} - 2.0685\right) \tag{23}$$

where, μ_r' is the relative permeability of the unknown sample and Δf the frequency shift (MHz).

Similarly, the tangent loss is varied from 0.001 to 0.1, and the shifts in transmission coefficients are observed as shown in Fig. 8. The empirical formula derived using Equations (1)–(15), (21) and process explained in [37] to calculate tangent loss of a unknown material is given by,

$$\tan\delta = \frac{1}{0.71764\ \mu_r'}\log\left(\frac{S_{21} + 53.1244 + 0.137 \times 10^{0.153\mu_r'}}{|-8.3142 + 0.7364\ \mu_r'|}\right) \tag{24}$$

where, S_{21} is transmission coefficient (dB).

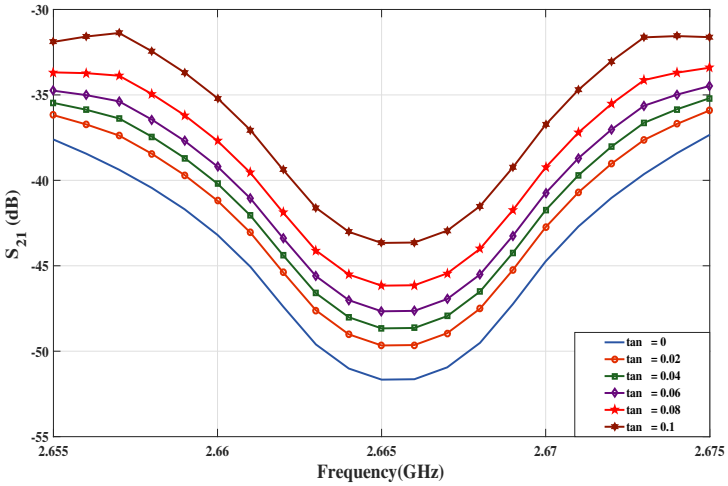

Figure 8. Variation of S_{21} (dB) magnitude of sensor with loss tangent value ranging from 0 to 0.1 for $\mu_r = 6$.

Due to higher magnetic field, spacing between inner diameters of the inductor is an effective position for addition of a sample with significant permeability. Addition of a sample with permeability changes magnetic coupling and causes a shift in even-mode resonant frequency only. Addition of a sample with significant relative permeability between IDC fingers results in no change in frequency response due to weak magnetic field.

3.2. Addition of Sample with Significant Relative Permittivity

The dielectric samples (rubber, plastic, white marble, magnetite and ferrite) are added, and the corresponding resonant frequency shifts are observed for each relative permittivity value compared to the unloaded case of the sensor as shown in Fig. 9. Moreover, the magnitude of odd-mode frequency shift is proportional to the permittivity value of the sample. Table 2 gives details of the frequency shift for various test samples. After observation of different frequency shifts in resonant frequency for variation in permittivity, the empirical formula derived by using Eqs. (1)–(15), (22) and process explained in [37] for determining the real part of permittivity of an unknown sample is given by,

$$\epsilon_r' = \frac{1}{0.7712}\left(10^{(1.5725 - 2\log(2.36006 - 0.02015 \times \Delta f))} - 4.984\right) \tag{25}$$

where, ϵ_r' is the relative permittivity of the unknown sample and Δf the frequency shift (MHz).

Tangent loss is varied from 0.001 to 0.1, and the corresponding shift in transmission coefficient is observed as shown in Fig. 10. The empirical formula for determining the tangent loss of permittivity is

given by,

$$\tan\delta = \left(\frac{1}{-0.41285 - 3.217\ \epsilon'_r + 0.5837\ \epsilon'^2_r}\right) \times \left(\left|\frac{S_{21} + 43.5341 + 0.16775\ \epsilon'_r}{0.8137 - 0.673\ \epsilon'_r}\right|\right) \tag{26}$$

where S_{21} is the transmission coefficient (dB).

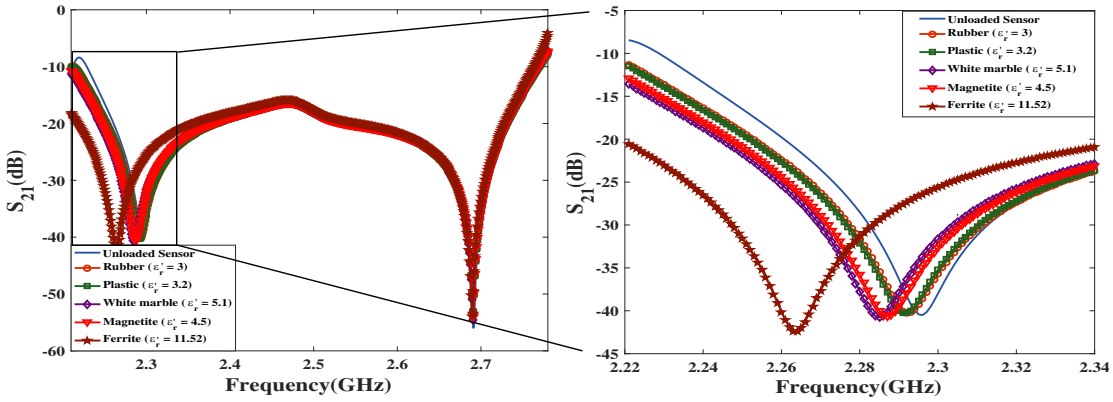

Figure 9. Frequency response of the sensor before and after addition of sample with different permittivity value.

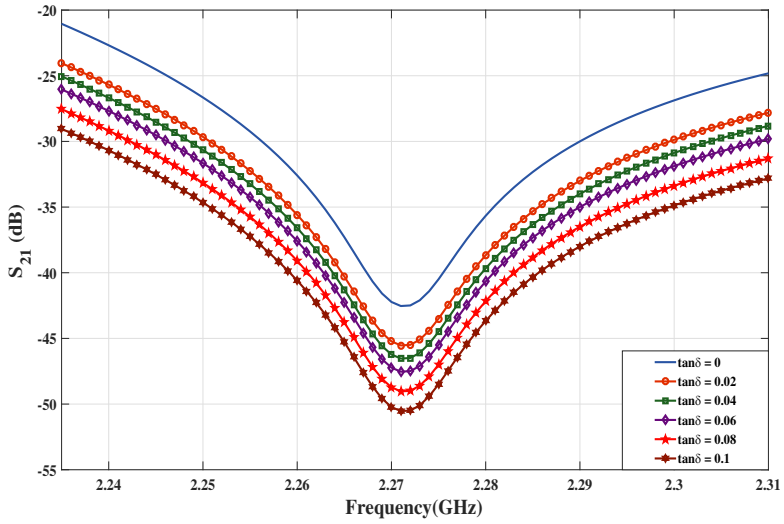

Figure 10. Variation of S_{21} (dB) magnitude of sensor with loss tangent value ranging from 0 to 0.1 for $\epsilon_r = 8$.

Table 2. Odd mode resonant frequency shifts after addition of different permittivity.

Test samle	Relative permittivity	Odd mode resonant frequency Shift
Rubber	3	6 MHz
Plastic	3.2	8 MHz
White marble	5.1	15.5 MHz
Magnetite	4.5	12.5 MHz
Ferrite (F22)	11.52	36 MHz

The gap between IDC fingers is an effective position for addition of a sample with significant permittivity due to higher electric field. Addition of a sample with significant permittivity changes IDC capacitance and causes a shift in odd-mode resonant frequency only. Due to weak electric field, no significant change in the frequency response is observed after the addition of a sample with significant relative permittivity between the inductor spacing.

4. MEASUREMENT AND RESULTS

The sensor is fabricated using a standard photolithography technique on a commercially available 1.6 mm FR-4 substrate with a conductive copper film coating of 35 µm. Geometric pattern from a photo-mask with the help of light-sensitive chemical photoresist is developed on the substrate, and the exposure pattern is engraved into the desired conductive film pattern. A pair of 50 Ω SMA connectors is then mounted on the fabricated sensor through the mechanical welding for the measurement of reflection and transmission data. The fabricated sensor (front and back view) and measurement setup are shown in Figs. 11(a), 11(b) and 11(c), respectively. The fabricated planar sensor length is 44 mm, and its width is 24 mm. The sensor is connected with the vector network analyzer (VNA) through coaxial SMA connectors. All the measurements are performed using the Agilent N2293A Network Analyzer. The input power taken is 0 dBm, and number of sweep points is taken as 10001.

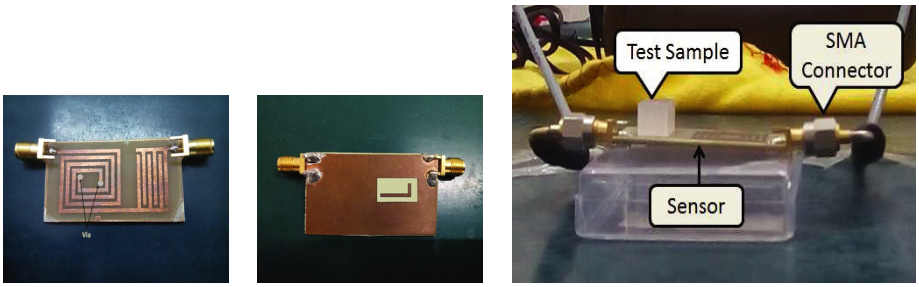

(a) (b) (c)

Figure 11. (a) Top view of fabricated sensor. (b) Bottom view of fabricated sensor. (c) Experimental setup.

After experimental setup, various material samples are added in the spacing between inductors and IDC fingers. Samples are placed in the specified area (gap between two inductors) to avoid direct contact with inductor metal layer. This placement position helps to find accurate results without any short connection. Shifts in the resonant frequency and S_{21} (dB) magnitude are measured using VNA as shown in Figs. 12 and 13. The measured resonant frequency and the transmission coefficient for each specimen are then fitted into the developed numerical model, and the corresponding relative permeability, relative permittivity and loss tangents are calculated using Eqs. (23), (24), (25) and (26), respectively, and shown in Tables 3 and 4. The measured results are also compared with standard

Table 3. Measured complex permeability using proposed sensor.

	Resonant frequency (GHz)	S_{21} **(dB)**	**Reference value** [38–41]		**Measured data**		**Percentage error**	
MUT ↓			μ_r'	$\tan\delta$	μ_r'	$\tan\delta$	$\%\mu_r'$	$\%\tan\delta$
Magnetite (Fe_3O_4)	2.692	−45.154	1.6	0.0268	1.6395	0.02753	2.468	2.72388
Soft cobalt steel (SAE 1018)	2.672	−48.3357	4.976	0.01039	4.924	0.01085	1.045	4.427
Ferrite core (F22)	2.651	−45.451	19	—	18.9999	0.0531	0.00052	—

available data, and the error percentage is calculated. From Tables 3 and 4, the results of complex permittivity and permeability measurement using the proposed sensor are analogous with the standard values available in the literature [38–43].

Measurements of the real part and tangent loss of permeability and permittivity are possible with

Table 4. Measured complex permittivity using proposed sensor.

	Resonant frequency (GHz)	S_{21} **(dB)**	**Reference value** [38–43]		**Measured data**		**Percentage error**	
MUT ↓			ϵ_r'	$\tan\delta$	ϵ_r'	$\tan\delta$	$\%\epsilon_r'$	$\%\tan\delta$
Rubber	2.298	−43.64	3.00	0.1639	3.1	0.157	3.333	4.209
Plastic	2.296	−46.0537	3.2	0.445	3.233	0.456	1.045	2.4719
White marble	2.289	−39.44	5.1	——	4.985	0.0095	2.342	——
Magnetite	2.292	−44.03	4.5	——	4.32	0.031675	4.00	——
Ferrite (F22)	2.2685	−38.87	11.52	——	11.411	0.0235	0.946	——

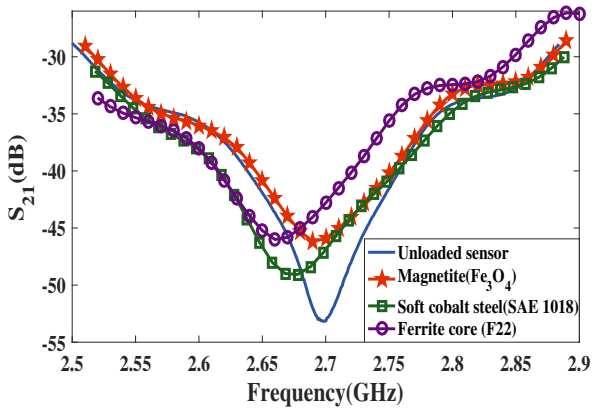

Figure 12. Measured Even mode frequency response for various magnetic samples.

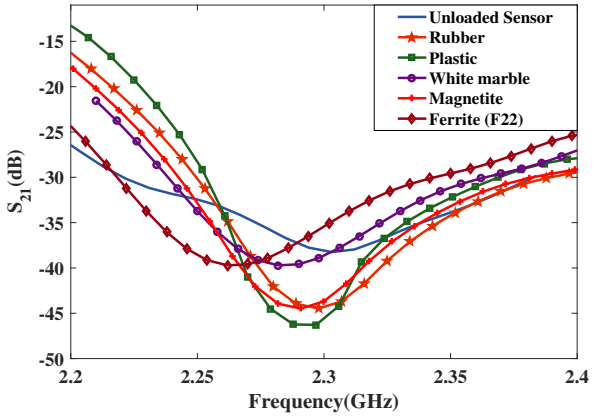

Figure 13. Measured odd mode frequency response for various dielectric samples.

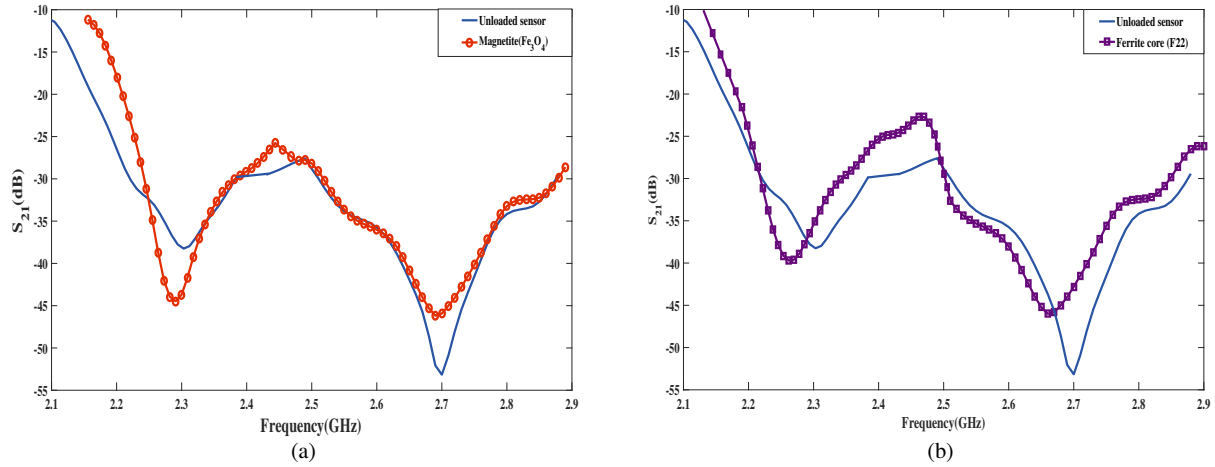

Figure 14. Frequency response of sensor after placement of (a) magnetite (b) ferrite (F22) between IDC fingers and inductor at the same time.

typical error between the range of 2%–5%. The error is obtained due to slight mismatch between simulated and fabricated designs.

After testing of sensor, a ferrite sample is added at both positions simultaneously. (i.e., spacing between inductor and IDC fingers). As ferrite composite posses magnetic and dielectric properties, significant shifts in both even mode and odd mode resonant frequencies are observed. Due to different permeability and permittivity values of ferrite, shifts in the resonant frequencies are different. Similarly, magnetite also exhibits magnetic and dielectric properties, and the corresponding permeability, permittivity and corresponding losses are measured. From Figs. 14(a) and 14(b), it is ensured that the proposed sensor allows real time, simultaneous and label-free measurement of permeability and permittivity of unknown sample.

5. TEST SAMPLE SIZE AND THICKNESS ANALYSIS

The consideration of the size and thickness of the test sample between sensitive part of the sensor is quite important for accurate measurement of the complex permeability and permittivity. 32 mm^2 and 80 mm^2 are the maximum effective area for placement of magnetic and dielectric test samples, respectively. The size of the magnetic test sample is varied from 2 mm^2 to 32 mm^2, and the corresponding shifts in resonant frequency and transmission coefficients are observed as shown in Fig. 15(a). Maximum shift and minimum transmission coefficient are observed for sample size of 32 mm^2. If sample size is further increased, then no change in frequency or transmission coefficient is observed. Similarly, thickness is varied from 0.03 mm to 2 mm, and no significant change in frequency and transmission coefficient is

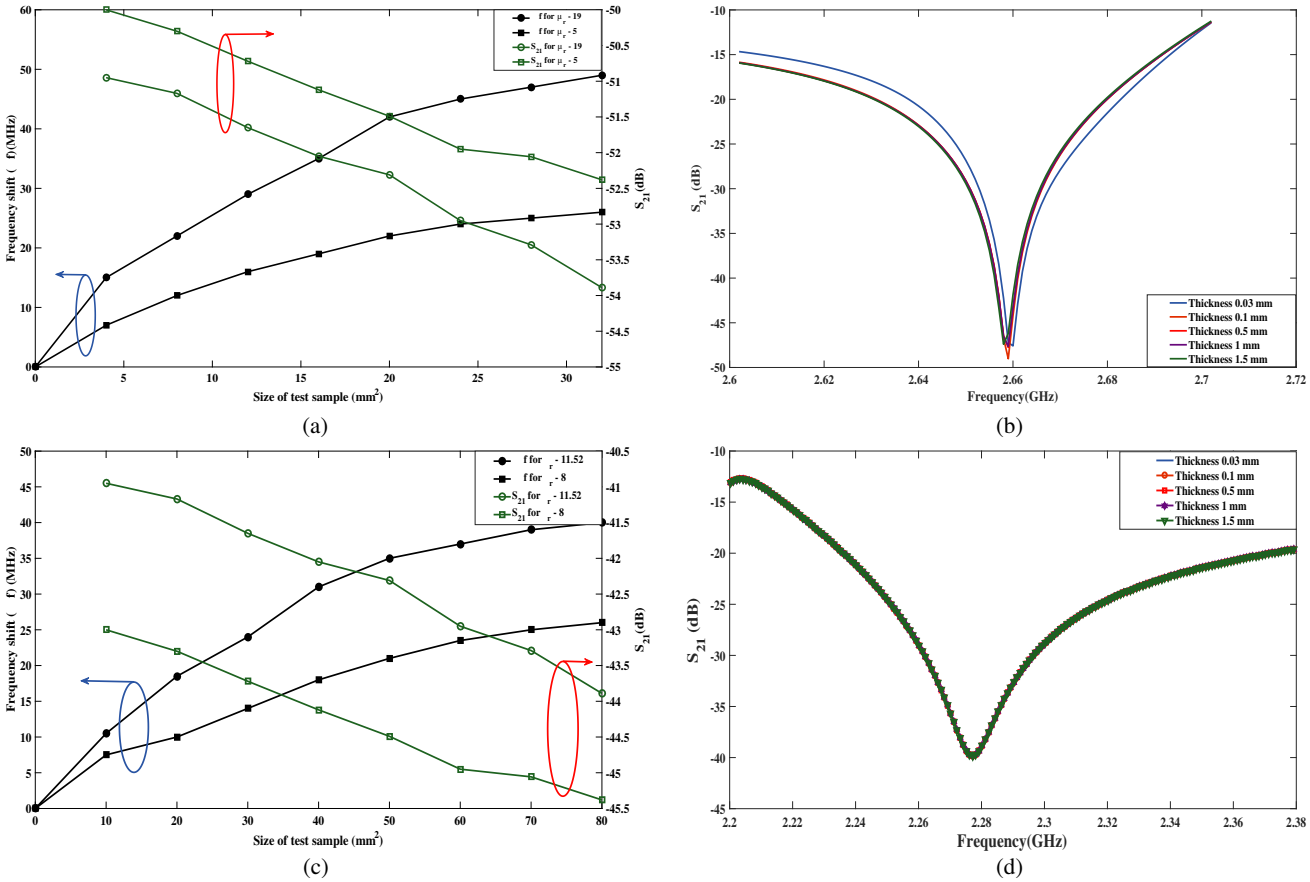

Figure 15. Response of the sensor for (a) size variation of magnetic test sample (b) thickness variation of magnetic test sample (c) size variation of dielectric test sample (d) thickness variation of dielectric test sample.

observed as shown in Fig. 15(b). From Figs. 15(c) and 15(d), it can be seen that variation in sample size of dielectric sample causes change in resonant frequencies and transmission coefficient, whereas thickness does not significantly affect frequency response of the sensor. Therefore, it is suggested that for accurate measurement results, sample size should cover effective area of the sensor.

Based on the data presented in Fig. 15, a numerical model is derived here using the curve fitting technique for the real permeability and permittivity in term of the resonant frequency, and the sample size is given by,

$$\mu_r' = \frac{1}{1.16}\left(\frac{30.7648}{(1.66629 - 0.022937\Delta f)^2(\sqrt[3]{S_{mz}})} - 2.0685\right) \tag{27}$$

$$\epsilon_r' = \frac{1}{0.086222\sqrt{S_{ez}}}\left(10^{(1.5725 - 2\log(2.36006 - 0.02015\times\Delta f))} - 4.984\right) \tag{28}$$

where, S_{mz} and S_{ez} are size of magnetic and dielectric sample in (mm^2), respectively.

6. CONCLUSION

In this paper, an appealing spiral inductor and IDC based planar resonant sensor have been designed and developed for simultaneous detection of permittivity and permeability of a sample with a single step measurement. The proposed sensor of size $44 \times 24\,\text{mm}^2$ and fabricated on a 1.6 mm FR-4 substrate operates in the frequency band ranging from 2.2 to 2.8 GHz. The developed sensor model has an advantage of differentiating permittivity and permeability based on the odd- and even-mode resonant frequencies. A numerical model has been developed for determining the relative permittivity, relative permeability and corresponding loss factor of the unknown sample. The measurement using various standard samples using the proposed sensor ensures that typical error is 3%. The proposed method is an ideal technique for microwave sensing and characterization of the sample commonly used in microwave planar circuits, as it is nondestructive and an economical method to measure the permittivity and permeability.

REFERENCES

1. Turi, E., *Thermal Characterization of Polymeric Materials*, Elsevier, 2012.
2. Petcharoen, K and A. Sirivat, "Synthesis and characterization of magnetite nanoparticles via the chemical co-precipitation method," *Materials Science and Engineering: B*, Vol. 177, No. 5, 421–427, 2012.
3. Ghosh Chaudhuri, R. and S. Paria, "Core/shell nanoparticles: Classes, properties, synthesis mechanisms, characterization, and applications," *Chemical Reviews*, Vol. 112, No. 4, 2373–2433, 2011.
4. Kim, J., A. Babajanyan, A. Hovsepyan, K. Lee, and B. Friedman, "Microwave dielectric resonator biosensor for aqueous glucose solution," *Review of Scientific Instruments*, Vol. 79, No. 8, 086107, 2008.
5. Kim, Y.-I., Y. Park, and H. K. Baik, "Development of LC resonator for label-free biomolecule detection," *Sensors and Actuators A: Physical*, Vol. 143, No. 2, 279–285, 2008.
6. Chitty, G. W., R. H. Morrison, Jr., E. O. Olsen, J. G. Panagou, and P. M. Zavracky, "Resonant sensor and method of making same," US Patent 4,764,244, August 16, 1988.
7. Akhter, Z. and M. J. Akhtar, "Free-space time domain position insensitive technique for simultaneous measurement of complex permittivity and thickness of lossy dielectric samples," *IEEE Transactions on Instrumentation and Measurement*, Vol. 65, No. 10, 2394–2405, 2016.
8. Zinal, S. and G. Boeck, "Complex permittivity measurements using TE/sub 11p/modes in circular cylindrical cavities," *IEEE Transactions on Microwave Theory and Techniques*, Vol. 53, No. 6, 1870–1874, 2005.
9. Ganguly, P., D. E. Senior, A. Chakrabarti, and P. V. Parimi, "Sensitive transmit receive architecture for body wearable RF plethysmography sensor," *2016 Asia-Pacific Microwave Conference (APMC)*, 1–4, 2016.

10. Zelenchuk, D. and V. Fusco, "Dielectric characterisation of PCB materials using substrate integrated waveguide resonators," *2010 European IEEE Microwave Conference (EuMC)*, 1583–1586, 2010.
11. Mikolaj, A. and A. F. Jacob, "Substrate integrated resonant near-field sensor for material characterization," *2010 IEEE MTT-S International Microwave Symposium Digest (MTT)*, 628–631, 2010.
12. Lee, H.-J., J.-H. Lee, H.-S. Moon, I.-S. Jang, J.-S. Choi, J.-G. Yook, and H.-I. Jung, "A planar split-ring resonator-based microwave biosensor for label-free detection of biomolecules, *Sensors and Actuators B: Chemical*, Vol. 169, 26–31, 2012.
13. Withayachumnankul, W., K. Jaruwongrungsee, C. Fumeaux, and D. Abbott, "Metamaterial-inspired multichannel thin-film sensor, *IEEE Sensors Journal*, Vol. 12, No. 5, 1455–1458, 2012.
14. Horestani, A. K., C. Fumeaux, S. F. Al-Sarawi, and D. Abbott, "Displacement sensor based on diamond-shaped tapered split ring resonator," *IEEE Sensors Journal*, Vol. 13, No. 4, 1153–1160, 2013.
15. Shafi, K. M., A. K. Jha, and M. J. Akhtar, "Improved planar resonant RF sensor for retrieval of permittivity and permeability of materials," *IEEE Sensors Journal*, Vol. 17, No. 17, 5479–5486, 2017.
16. Ebrahimi, A., W. Withayachumnankul, S. Al-Sarawi, and D. Abbott, "High-sensitivity metamaterial-inspired sensor for microfluidic dielectric characterization," *IEEE Sensors Journal*, Vol. 14, No. 5, 1345–1351, 2014.
17. Chen, C.-M., J. Xu, and Y. Yao, "SIW resonator humidity sensor based on layered black phosphorus," *Electronics Letters*, Vol. 53, No. 4, 249–251, 2017.
18. Varshney, P. K., N. K. Tiwari, and M. J. Akhtar, "SIW cavity based compact RF sensor for testing of dielectrics and composites," *2016 IEEE MTT-S International Microwave and RF Conference (IMaRC)*, 1–4, 2016.
19. Cui, Y., A. K. Kenworthy, M. Edidin, R. Divan, D. Rosenmann, and P. Wang, "Analyzing single giant unilamellar vesicles with a slotline-based RF nanometer sensor," *IEEE Transactions on Microwave Theory and Techniques*, Vol. 64, No. 4, 1339–1347, 2016.
20. Amin, E. M. and N. C. Karmakar, "A passive RF sensor for detecting simultaneous partial discharge signals using time-frequency analysis," *IEEE Sensors Journal*, Vol. 16, No. 8, 2339–2348, 2016.
21. Hettak, K., N. Dib, A.-F. Sheta, and S. Toutain, "A class of novel uniplanar series resonators and their implementation in original applications," *IEEE Transactions on Microwave Theory and Techniques*, Vol. 46, No. 9, 1270–1276, 1998.
22. Samavati, H., A. Hajimiri, A. R. Shahani, G. N. Nasserbakht, and T. H. Lee, "Fractal capacitors," *IEEE Journal of Solid-State Circuits*, Vol. 33, No. 12, 2035–2041, 1998.
23. Yue, C. P., C. Ryu, J. Lau, T. H. Lee, and S. S. Wong, "A physical model for planar spiral inductors on silicon, *International Electron Devices Meeting, 1996, IEDM'96*, 155–158, 1996.
24. Chretiennot, T., D. Dubuc, and K. Grenier, "A microwave and microfluidic planar resonator for efficient and accurate complex permittivity characterization of aqueous solutions," *IEEE Transactions on Microwave Theory and Techniques*, Vol. 61, No. 2, 972–978, 2013.
25. Bojanic, R., V. Milosevic, B. Jokanovic, F. Medina-Mena, and F. Mesa, "Enhanced modelling of split-ring resonators couplings in printed circuits," *IEEE Transactions on Microwave Theory and Techniques*, Vol. 62, No. 8, 1605–1615, 2014.
26. Facer, G., D. Notterman, and L. Sohn, "Dielectric spectroscopy for bioanalysis: From 40 Hz to 26.5 GHz in a microfabricated wave guide," *Applied Physics Letters*, Vol. 78, No. 7, 996–998, 2001.
27. Altunyurt, N., M. Swaminathan, P. M. Raj, and V. Nair, "Antenna miniaturization using magneto-dielectric substrates," *59th Electronic Components and Technology Conference, 2009, ECTC 2009*, 801–808, 2009.
28. Han, K., M. Swaminathan, P. M. Raj, H. Sharma, K. Murali, R. Tummala, and V. Nair, "Extraction of electrical properties of nanomagnetic materials through meander-shaped inductor and inverted-F antenna structures," *2012 IEEE 62nd Electronic Components and Technology Conference (ECTC)*,

1808–1813, 2012.

29. Kim, J. W., "Development of interdigitated capacitor sensors for direct and wireless measurements of the dielectric properties of liquids," https://repositories.lib.utexas.edu/handle/2152/10565, 2008.
30. Hong, J.-S. G. and M. J. Lancaster, *Microstrip Filters for RF/Microwave Applications*, Vol. 167, John Wiley & Sons, 2004.
31. Jenei, S., B. K. Nauwelaers, and S. Decoutere, "Physics-based closed-form inductance expression for compact modeling of integrated spiral inductors," *IEEE Journal of Solid-State Circuits*, Vol. 37, No. 1, 77–80, 2002.
32. Asgaran, S., "New accurate physics-based closed-form expressions for compact modeling and design of on-chip spiral inductors," *The 14th International Conference on IEEE Microelectronics, 2002-ICM*, 247–250, 2002.
33. Fooks, E. H. and R. A. Zakarevicius, *Microwave Engineering Using Microstrip Circuits*, Prentice-Hall, Inc., 1990.
34. Smith, D. and D. Schurig, "Electromagnetic wave propagation in media with indefinite permittivity and permeability tensors," *Physical Review Letters*, Vol. 90, No. 7, 077405, 2003.
35. Ishimaru, A., *Wave Propagation and Scattering in Random Media*, Vol. 2, 1978.
36. Garg, R., I. Bahl, and M. Bozzi, *Microstrip Lines and Slotlines*, Artech House, 2013.
37. Baker-Jarvis, J., E. J. Vanzura, and W. A. Kissick, "Improved technique for determining complex permittivity with the transmission/reflection method," *IEEE Transactions on Microwave Theory and Techniques*, Vol. 38, No. 8, 1096–1103, 1990.
38. Cuenca, J. A., K. Bugler, S. Taylor, D. Morgan, P. Williams, J. Bauer, and A. Porch, "Study of the magnetite to maghemite transition using microwave permittivity and permeability measurements," *Journal of Physics: Condensed Matter*, Vol. 28, No. 10, 106002, 2016.
39. Tokpanov, Y., V. Lebedev, and W. Pellico, "Measurements of magnetic permeability of soft steel at high frequencies," *Proceedings of IPAC-2012*, New Orleans, Louisiana, USA, 2012.
40. Van Dam, R. L., J. M. Hendrickx, N. J. Cassidy, R. E. North, M. Dogan, and B. Borchers, "Effects of magnetite on high-frequency ground-penetrating radar," *Geophysics*, Vol. 78, No. 5, H1–H11, 2013.
41. Kaye, G. W. C. and T. H. Laby, *Tables of Physical and Chemical Constants: And Some Mathematical Functions*, Longmans, Green and Company, 1921.
42. Bapna, P. and S. Joshi, "Measurement of dielectric properties of various marble stones of Mewar region of Rajasthan at X-band microwave frequencies," *International Journal of Engineering and Innovative Technology (IJEIT)*, Vol. 2, 180–186, 2013.
43. *Dielectric Constant, Strength, & Loss Tangent*, 2006.